AIMS Mathematics

https://www.aimspress.com/journal/Math

AIMS Mathematics, 11(5): 14791–14819.
DOI: 10.3934/math.2026609
Received: 19 January 2026
Revised: 09 May 2026
Accepted: 13 May 2026
Published: 26 May 2026

Research article

Robust identification of multiple point targets in time-domain fluorescence diffuse optical tomography

Junyong Eom[1,†], **Jaeseung Kim**[2,†] **and Hwijae Son**[2,*]

[1] Graduate School of Science and Technology, Gunma University, Maebashi, Japan

[2] Department of Mathematics, Konkuk University, Seoul 05029, Republic of Korea

* **Correspondence:** Email: hwijaeson@konkuk.ac.kr; Tel: +821083807819.

Abstract: We present a reconstruction framework for time-domain fluorescence diffuse optical tomography (FDOT) to identify the locations of fluorescent point targets from boundary measurements. Unlike conventional approaches that rely on reduced temporal features, the proposed method utilizes the entire measured time-domain fluorescence response in the inverse reconstruction. The reconstruction is formulated as a gradient-based optimization problem in which candidate target locations are iteratively updated to match the observed temporal data. Numerical experiments demonstrate accurate and robust localization for both single- and multi-target configurations. Moreover, the proposed method remains effective when the number of targets is unknown a priori: In overparameterized reconstructions, redundant candidate points are automatically suppressed without the need for explicit regularization. This robustness makes the approach particularly suitable for practical FDOT settings, where the number of fluorescent targets is typically unknown. Furthermore, we demonstrate the practical feasibility of the framework through a comprehensive robustness analysis, confirming its stability under significant measurement noise and systematic mismatches in background optical properties. Finally, we show that the point-based optimization strategy can be successfully extended to localize extended volumetric targets and estimate their size, highlighting the versatility of the proposed method for complex geometric configurations.

Keywords: fluorescence diffuse optical tomography; inverse problems; full-waveform reconstruction; overparameterization; gradient-based optimization
Mathematics Subject Classification: 35R30, 65M32, 92C55

[†] These authors contributed equally to this work.

1. Introduction

Fluorescence diffuse optical tomography (FDOT) is a fluorescence imaging technique for fluorescence objects embedded in highly scattering media. In particular, this technique is essential in biological or medical applications for visualization of specific diseases and biological activities in vivo using fluorescent probes from measurements outside of the tissue [1–3]. Since the problems caused by the highly scattering media do not allow for visualizing fluorescence objects in deep tissue using standard imaging techniques such as a fluorescence camera, a special imaging technique, FDOT, is required. In highly scattering media such as biological tissue, the light path is no longer straight, and repeated scattering makes the light propagation an energy dissipation process, approximately described by a diffusion equation. The image of the objects is blurred significantly. Eventually, a reconstruction method based on the light propagation model is required to visualize and recover the quantitative information of the three-dimensional fluorescence distribution from the measurements only on the boundary of the medium [4, 5].

In this paper, we focus on a time-domain method of FDOT, using temporal response functions of fluorescence. The temporal response function of fluorescence is the time course of fluorescence intensity after an instantaneous injection of excitation light, like a delta function. After the injection, the excitation light spreads in the medium, and then the fluorophores in the fluorescence objects absorb the excitation light. The fluorescence emitted from the fluorophores after a specific time, known as the fluorescence lifetime, spreads from the position of the fluorophores and finally arrives at the detection point. Many different paths of the excitation and fluorescence light correspond to different arrival times at the object and the detector [6]. Therefore, the temporal response function is determined by the path length distribution and the fluorescence lifetime, which reveals the distance information between the object and the excitation and detection points.

Next, we start to formulate our inverse problem. Let $\Omega = \mathbb{R}^3_+ := \{(x, y, z) \mid x, y \in \mathbb{R}, z > 0\}$ and denote its boundary by $\partial\Omega$. Excitation and emission processes, u_e and U_m, respectively, can be modeled as the following coupled diffusion equations [7]:

$$\begin{cases} \left(v^{-1}\partial_t - D\Delta + \mu_a\right) u_e = 0, & (x, t) \in \Omega \times (0, \infty), \\ u_e = 0, & (x, t) \in \bar{\Omega} \times \{0\}, \\ \partial_\nu u_e + \beta u_e = \delta(x - x_s)\,\delta(t), & (x, t) \in \partial\Omega \times (0, \infty) \end{cases} \tag{1.1}$$

and

$$\begin{cases} \left(v^{-1}\partial_t - D\Delta + \mu_a\right) U_m = \mu(f_\ell * u_e), & (x, t) \in \Omega \times (0, \infty), \\ U_m = 0, & (x, t) \in \bar{\Omega} \times \{0\}, \\ \partial_\nu U_m + \beta U_m = 0, & (x, t) \in \partial\Omega \times (0, \infty). \end{cases} \tag{1.2}$$

Here, $\partial_\nu := \nu \cdot \nabla$ is the exterior normal derivative, v is the speed of light in the medium, D is the diffusion constant, μ_a is the absorption coefficient, and $\beta = b/D > 0$ is a positive constant with $b \in [0, 1]$, coming from the Fresnel reflection at the boundary due to the refractive index mismatch. In addition, $\delta(\cdot)$ denotes the delta function, and $x_s \in \partial\Omega$ is the position of the point source where the excitation light is injected. Further, the source term, which corresponds to the fluorescence emission from the fluorophores, for U_m on the right-hand side of (1.2) is given as

$$\mu(f_\ell * u_e)(x, t) := \mu(x) \int_0^t \ell^{-1} e^{-\frac{t-s}{\ell}} u_e(x, s; x_s)\, \mathrm{d}s, \tag{1.3}$$

where $\mu(x) > 0$ is the absorption coefficient of a fluorophore, and $f_\ell * u_e$ is the convolution of u_e and the fluorescence decay function, $f_\ell(t) := \ell^{-1}e^{-t/\ell}$, $t \geq 0$, with the fluorescence lifetime $\ell > 0$. Note that if $\ell \to 0$, it is easy to see that $\mu(f_\ell * u_e)(x,t) = \mu(x)u_e(x,t;x_s)$. Hence, we extend the definition of (1.3) to the case of the zero fluorescence lifetime ($\ell = 0$) by defining its right-hand side by $\mu(x)u_e(x,t;x_s)$. In the above formulation, D and μ_a are space-dependent in general. However, some studies suggest that the reconstruction results of FDOT are less sensitive to the heterogeneity of these parameters [8]. Thus, we assume these parameters are constant to idealize the problem as in other FDOT studies [9,10].

We formulate the inverse problem as follows. Supposing that $\mu(x)$ is unknown, and it is either supported at a single point target or multiple point targets. Here, the form of $\mu(x)$ is either $\mu(x) = c\,\delta(x - x_c)$ or $\mu(x) = \sum_{j=1}^{J} c_j\delta(x - x_{c_j})$ corresponding to either that it is supported at a single target point x_c or multiple point targets $\{x_{c_j}\}_{j=1}^{J}$. Then, we aim to identify the locations of the point targets from the time-dependent boundary measurement data

$$\left\{U_m(x_d^{(n)}, t; x_s^{(n)}) : n = 1, \cdots, N.\right\}, \tag{1.4}$$

where $\{(x_s^{(n)},\ x_d^{(n)}) \mid n = 1,\ 2,\ \cdots,\ N\}$ are N sets of source and detector pairs (S–D pairs) consisting of source points $\{x_s^{(n)}\}_{n=1}^{N}$ and detector points $\{x_d^{(n)}\}_{n=1}^{N}$ on $\partial\Omega$. Throughout this work, we assume that the fluorescence absorption coefficient is supported at a finite number of points and that the corresponding intensity coefficients are known. Accordingly, the inverse problem is formulated as the identification of the target locations only, while the fluorescence intensities are treated as fixed parameters.

To the best of our knowledge, existing time-domain FDOT reconstruction methods can be broadly divided into two categories: peak-time-based approaches [11–13] and moment-based approaches [14–16]. Peak-time-based methods have the advantage of admitting a clear mathematical interpretation through asymptotic analysis; however, their applicability becomes limited when multiple point targets are present, particularly in determining the number of targets. Moment-based approaches provide another useful framework since time-domain convolutions can be expressed in terms of temporal moments. On the other hand, improving reconstruction resolution typically requires higher-order moments, and the computed moments may depend on the temporal discretization of the measurements and on the choice of the integration interval. In contrast, the proposed framework does not rely solely on a single temporal feature such as the peak time or on a finite number of temporal moments. Rather, it exploits the exponentially fast decay of the contributions associated with redundant candidates as the distance parameter becomes large, and uses this property to distinguish candidate points corresponding to the true targets from redundant ones within an overparameterized setting. Therefore, the main novelty of the present work lies not in introducing a new optimization formulation, but in the decay-based suppression mechanism for redundant candidates, with overparameterization serving as the computational framework in which this mechanism operates.

We conduct a series of numerical experiments to examine how the full time-domain measurements $U_m(t)$ encode the geometric configuration of fluorescent targets and to assess whether their locations can be reliably recovered under different structural assumptions. We consider three representative reconstruction scenarios.

First, we study the case in which the fluorescence distribution is supported at a single point target located at x_c. For each S–D pair, the entire temporal response $U_m(t)$ is computed, and the reconstruction model utilizes the full-waveform data $U_m(t)$ to estimate the single unknown target location.

Second, we consider multiple point targets. In this case, the measured time-domain data is given by the superposition of the responses generated by the fluorescent sources, leading to more complex temporal signatures. The reconstruction model is then assessed by simultaneously recovering multiple target locations from the full time-resolved measurements.

Finally, we examine a more general and practically relevant scenario in which the number of fluorescent targets is unknown a priori. In this setting, the measured data may be generated by one or more point targets, but the reconstruction is deliberately performed using an overparameterized model in which the number of candidate variables K exceeds the true number of targets J. This setup mimics realistic situations in which only boundary measurements are available and no prior information on target multiplicity is provided. The objective of this experiment is to investigate whether the proposed reconstruction method can naturally suppress redundant candidates and identify the effective target structure encoded in the temporal measurements across different levels of target multiplicity.

In addition to these structural configurations, we further investigate the robustness of the proposed framework under measurement noise by performing overparameterized reconstructions using noisy time-domain data. Together, these experiments provide a systematic evaluation of the proposed full-waveform reconstruction approach in both noise-free and noisy settings.

The overall numerical simulation and reconstruction framework is illustrated in Figure 1. As shown in the figure, our approach consists of two primary components: (i) a forward model that generates the time-domain boundary measurements from the target configuration, and (ii) a full-waveform reconstruction strategy that iteratively updates K candidate locations to match the observed waveforms. This illustration highlights how the proposed framework effectively distinguishes the effective target structure from redundant candidates, which are naturally suppressed during the iterative reconstruction process as they migrate toward regions of negligible signal contribution.

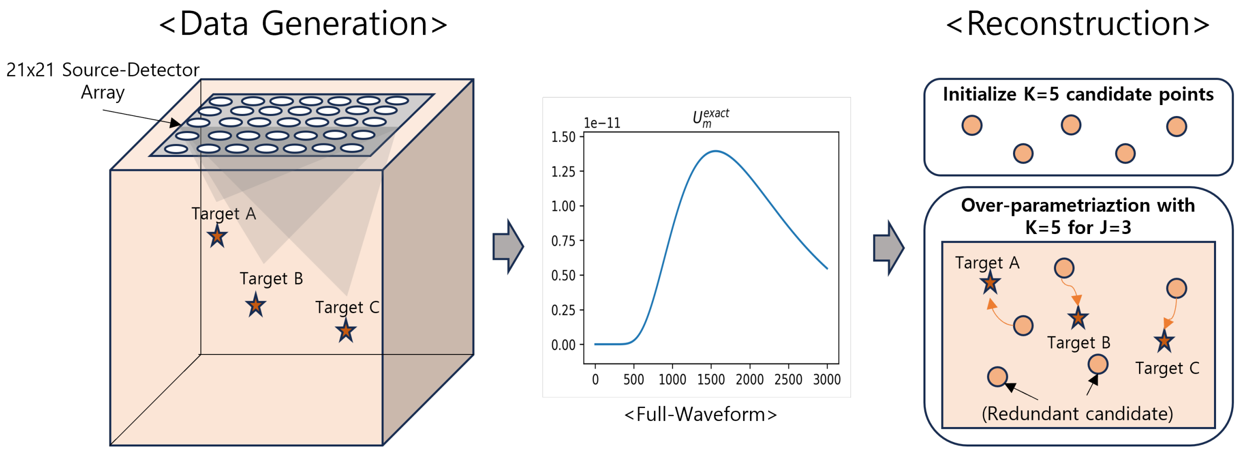

Figure 1. Schematic of the numerical simulation and reconstruction framework. (Left) The computational domain with a 21×21 source–detector array and embedded fluorescent point targets. (Middle) Representative time-resolved fluorescence waveform $U_m^{\text{exact}}(t)$ generated from the setup. (Right) The full-waveform reconstruction strategy utilizing an overparameterized set of candidate points; effective candidates converge to the true targets, while redundant candidates are naturally suppressed during the iterative process.

2. Expression for the solution and asymptotic behavior

In this section, we first give the expression for the solution and then derive the asymptotic behavior of the solution. When there is a single point target x_c in Ω, and a S–D pair $(x_s,\ x_d)$ is placed on $\partial\Omega$, zero fluorescence lifetime solution ($\ell = 0$) to (1.2) is given as

$$u_m(x_d,t;x_s) = \frac{ce^{-v\mu_a t}}{16\pi^3 D^2 v}\int_0^t ((t-s)s)^{-\frac{3}{2}} e^{-\frac{|x_d-x_c|^2}{4vD(t-s)}} e^{-\frac{|x_s-x_c|^2}{4vDs}}\hat{\mathcal{K}}(x_{c_3};t-s)\hat{\mathcal{K}}(x_{c_3};s)\,\mathrm{d}s, \tag{2.1}$$

where

$$\begin{cases} \hat{\mathcal{K}}(x_{c_3};t) := 1-\beta\sqrt{\pi vDt}\,\exp\left(\left(\frac{x_{c_3}+2\beta vDt}{\sqrt{4vDt}}\right)^2\right)\mathrm{erfc}\left(\frac{x_{c_3}+2\beta vDt}{\sqrt{4vDt}}\right), \\ \mathrm{erfc}(\xi) = \frac{2}{\sqrt{\pi}}\int_\xi^\infty e^{-s^2}\,\mathrm{d}s, \quad \xi\in\mathbb{R}. \end{cases}$$

Here, $|\xi|$ is the Euclidean norm of any three-dimensional vector ξ, and x_{c_3} is the third component of the target x_c. See Section 2 of [17] for the derivation of (2.1) in detail. Then, the solution U_m to (1.2) is given as

$$U_m = \mathcal{K}*(\mu f_\ell * u_e) = f_\ell * (\mathcal{K}*[\mu u_e]) = f_\ell * u_m,$$

where $\mathcal{K}$ is the Green function associated with (1.2). Then, it becomes

$$U_m(x_d,t;x_s) = \int_0^t \ell^{-1}e^{-\frac{t-s}{\ell}}u_m(x_d,s;x_s)\,\mathrm{d}s. \tag{2.2}$$

In the next Lemma 2.1, one can see the asymptotic behavior of u_m when $\lambda \gg 1$, where $\lambda > 0$ is the distance parameter determined in terms of the distances between the source, the target, and the detector as

$$\lambda^2 = \frac{|x_d-x_c|^2+|x_s-x_c|^2}{2vD}. \tag{2.3}$$

Lemma 2.1. *Let $x_d,\ x_s \in \partial\Omega$, and assume that*

$$\left||x_d-x_c|^2-|x_s-x_c|^2\right| \le Ct \quad \text{for some} \quad C>0.$$

Define λ as in (2.3) *and $k := v\mu_a$. Then, u_m satisfies*

$$u_m(t) = u_m^a(t) + O\left(u_m^a(t)\lambda^{-1}\right) \ \textit{for}\ \lambda\gg 1,$$

where

$$\begin{aligned} u_m^a(t) &= C_0 e^{-kt}t^{-\frac{3}{2}}e^{-\frac{\lambda^2}{t}}\left(\frac{x_{c_3}}{x_{c_3}+\beta vDt}\right)^2 \\ \textit{with}\quad C_0 &:= \frac{c}{8\pi^{\frac{5}{2}}v^{\frac{1}{2}}D^{\frac{3}{2}}}\left(\frac{1}{|x_d-x_c|}+\frac{1}{|x_s-x_c|}\right). \end{aligned} \tag{2.4}$$

We provide a proof of Lemma 2.1 in non-dimensional form in the appendix. The asymptotic behavior of u_m in Lemma 2.1 provides a natural criterion for selecting successful approximations when the number of target points is unknown. In such settings, we intentionally introduce an overparameterized set of candidate points. Numerical observations show that, except for candidates corresponding to the true target locations, the remaining candidates exhibit monotonically increasing depth coordinates. By Lemma 2.1, this behavior implies that the associated distance parameter λ becomes large, and consequently the corresponding contributions u_m decay exponentially fast to zero. It is worth noting that an increase in the depth coordinate is equivalent to an increase in the distance parameter λ since the distance between S-D pair (x_d, x_s) is fixed in the experimental setting. As quantitatively illustrated in Figure 2, the approximately linear increase of λ with respect to the depth z leads to a rapid exponential decay of the signal intensity. Therefore, candidates whose waveform contributions vanish according to the asymptotic estimate in Lemma 2.1 can be regarded as spurious, while only those candidates that yield non-negligible u_m persist as valid approximations of the true targets.

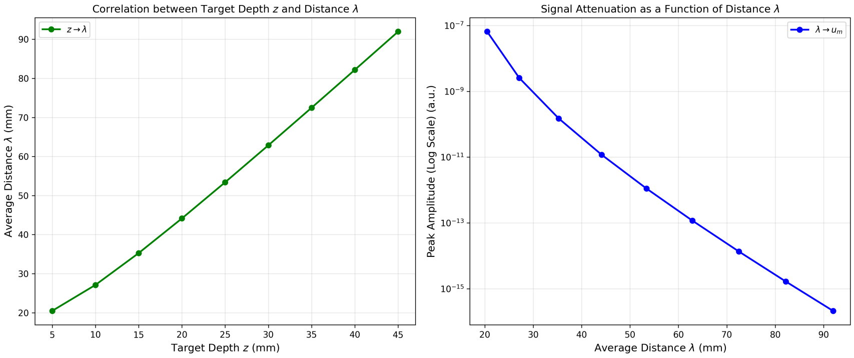

Figure 2. Quantitative validation of the signal attenuation characteristics described in Lemma 2.1. (Left) Linear correlation between the target depth z and the average distance parameter λ, establishing the geometric link. (Right) Exponential decay of the peak fluorescence intensity u_m as a function of λ. The log-scale plot demonstrates that the signal contribution diminishes exponentially fast as the distance increases, providing a physical basis for the suppression of redundant candidates at large depths.

3. Data generation

In this section, we describe the numerical procedure used to generate the synthetic time-domain fluorescence data. To represent typical optical properties of biological tissues, we employ standard FDOT parameters: $v = 0.219$ mm/ps, $D = 1/3$ mm, $\mu_a = 0.01$ mm^{-1}, $\beta = 0.5493$ mm^{-1}, and a fluorescence lifetime $\ell = 1000$ ps. A uniform array of 21×21 source–detector (S–D) pairs is positioned on the boundary $\partial\Omega$ as $\Xi = \{(x_s, x_d)^{(m,n)} = ((4+m, n, 0), (-4+m, n, 0)) : m, n = 0, \ldots, 20\}$, resulting in $N_{\mathrm{SD}} = 441$ pairs. The temporal domain is discretized into $T = 3001$ uniform steps over $[0, 3000]$ ps. For a prescribed set of point targets $\{x_{c,j}\}_{j=1}^{J}$, the zero-lifetime signal $u_m(t)$ is computed by numerically evaluating the integral representation (2.1) using a Gauss–Legendre quadrature with $Q = 120$ nodes. Due to the linearity of the forward model, the total response is obtained by a direct superposition, $u_m(t; \{x_{c,j}\}) = \sum_{j=1}^{J} u_m(t; x_{c,j})$, which is then organized into a matrix $u_m \in \mathbb{R}^{T \times N_{\mathrm{SD}}}$. Finally, the measured signal $U_m^{\mathrm{exact}}(t)$ incorporating a nonzero lifetime ℓ is obtained via the convolution $U_m(t) = \int_0^t \ell^{-1} e^{-(t-s)/\ell} u_m(s) ds$, implemented using a trapezoidal discretization of the decay kernel.

The precise formulation of this forward model is fundamental to the subsequent inverse reconstruction. By establishing a differentiable mapping between the target locations $x_{c,j}$ and the boundary measurements, this numerical framework allows the optimization process to directly exploit the temporal arrival times and peak structures of the waveforms. Furthermore, the capacity to accurately simulate the causal delay and diffusive broadening of the light pulse provides the necessary physical constraints to distinguish between multiple targets and effectively suppress redundant candidates during overparameterized reconstruction.

4. Inverse reconstruction method

We now present a full-waveform-based inverse reconstruction framework for recovering the locations of fluorescence targets from the synthetic time-domain data U_m^{exact} generated in Section 3. The reconstruction is formulated as an optimization problem in which the locations of candidate targets are iteratively adjusted so that the predicted temporal waveforms match the reference data.

Let $\{x_{c,j}^*\}_{j=1}^J \subset \Omega$ denote the true target locations. Let $\{\hat{x}_{c,j}\}_{j=1}^K \subset \Omega$ denote the candidate locations to be reconstructed. The number of candidates K does not necessarily coincide with the true number of targets J, and we allow $K \geq J$ to account for situations in which the number of inclusions is unknown.

For a given set of candidate locations $\{\hat{x}_{c,j}\}$, the forward model described in Section 3 produces a predicted time-domain waveform

$$U_m^{\text{pred}}(t; \{\hat{x}_{c,j}\}) \in \mathbb{R}^{T \times N_{\text{SD}}}, \tag{4.1}$$

which is compared with the reference waveform $U_m^{\text{exact}}(t)$. The inverse problem is to determine the candidate locations $\{x_{c,j}\}$ such that the predicted waveform matches the reference data in the least-square sense.

The reconstruction is carried out by minimizing the discrepancy between the predicted and reference temporal waveforms over all time steps and all S–D pairs. In practice, the magnitude of $U_m(t)$ is extremely small, which may lead to numerical instability when evaluating the loss function and its gradients. To improve numerical conditioning, a detector-wise normalization is applied to both the predicted and reference datasets.

Specifically, for each detector index p, we define the normalized signal

$$\widetilde{U}(t,p) = \frac{U(t,p) - \mu_p}{\sigma_p}, \qquad \mu_p = \frac{1}{T}\sum_{i=1}^{T} U(t_i,p), \quad \sigma_p^2 = \frac{1}{T}\sum_{i=1}^{T} \left(U(t_i,p) - \mu_p\right)^2.$$

The inverse reconstruction problem is then formulated as the following optimization problem:

$$\min_{\{\hat{x}_{c,j}\}_{j=1}^K \subset \Omega} \quad \mathcal{L}(\{\hat{x}_{c,j}\}) \tag{4.2}$$

where the objective functional $\mathcal{L}$ is defined by

$$\mathcal{L}(\{\hat{x}_{c,j}\}) = \frac{1}{T\,N_{\text{SD}}} \sum_{p=1}^{N_{\text{SD}}} \sum_{i=1}^{T} \left(\widetilde{U}_m^{\text{pred}}(t_i, p; \{\hat{x}_{c,j}\}) - \widetilde{U}_m^{\text{exact}}(t_i, p)\right)^2. \tag{4.3}$$

This objective measures the mean squared discrepancy between the predicted and reference waveforms over all time steps and all S–D pairs. Since the forward model is differentiable with respect to the candidate locations $\{\hat{x}_{c,j}\}$, the optimization problem (4.2) is solved using gradient-based methods. In all numerical experiments, the candidate locations are updated using the Adam optimizer.

Notably, even when the number of candidate points exceeds the true number of fluorescence targets ($K > J$), only a subset of the candidates converges toward the actual target locations. The remaining candidates automatically migrate to regions that yield negligible contributions to the predicted waveform without requiring any explicit regularization or sparsity constraints. Therefore, this unified reconstruction framework is used for all numerical experiments presented in Section 5.

5. Numerical experiments

In this section, we present a series of reconstruction experiments based on the full-waveform data described in Section 3. We first evaluate the method in three representative scenarios: single-target reconstruction (Section 5.1), multiple-target reconstruction (Section 5.2), and overparameterized reconstruction with an unknown number of targets (Section 5.3). Furthermore, we assess the practical feasibility and robustness of the framework through a comprehensive analysis of its performance under measurement noise and optical property mismatches (Section 5.4), as well as its capacity to reconstruct extended volumetric inclusions (Section 5.5). In all cases, the reconstruction method described in Section 4 is applied without any modification.

5.1. Single-target reconstruction

We first consider the reconstruction of a single fluorescent point target. The true target is located at $x_c^* = (8, 12, 20)$, and the corresponding reference waveform U_m^{exact} is generated using the forward model described in Section 3. The reconstruction is performed using a single candidate point ($K = 1$), whose location is optimized via the full-waveform matching method introduced in Section 4. In all experiments, the initial candidate location is randomly sampled from the interior of the domain, without prior knowledge of the true target location.

Table 1 summarizes the single-target reconstruction results obtained from multiple independent runs with different initializations. For the target at $x_c^* = (8, 12, 20)$, five initial positions are selected over a wide spatial range. Despite the variability in the initial guesses, all reconstructions converge to the same recovered location, which agrees with the ground truth up to small numerical errors.

Table 1. Single-target reconstruction results for various initializations. For each target location x_c^*, the reconstruction is performed using a single candidate point ($K = 1$) initialized at different positions within the domain. The table reports the recovered location and the corresponding absolute reconstruction error.

Target	*Initial*	*Prediction*	*Absolute Err*
8, 12, 20	2, 2, 5	8.00000, 11.99998, 19.99996	3.79197e-05
	5, 5, 17	8.00000, 11.99999, 20.00000	1.90734e-05
	14, 7, 25	8.00000, 12.00000, 20.00000	0.0
	16, 15, 20	8.00000, 11.99992, 20.00006	1.00539e-04
	20, 20, 30	7.99999, 12.00002, 20.00000	2.63946e-05
5, 5, 20	2, 2, 23	5.00000, 5.00000, 20.00000	0.0
	8, 8, 14	5.00000, 5.00000, 20.00000	0.0
10, 10, 16	4, 3, 17	10.00000, 9.99999, 16.00000	2.13248e-06
	12, 12, 14	10.00000, 10.00000, 16.00000	0.0

Additional experiments are conducted for targets located at $(5, 5, 20)$ and $(10, 10, 16)$ to verify that the observed convergence behavior is not specific to a single geometric configuration. In all cases, stable and accurate reconstruction is achieved, confirming the robustness of the method across different target locations.

The absolute reconstruction errors in Table 1 are typically on the order of 10^{-5} or smaller. In several cases, the error is reported as zero, which indicates agreement up to the numerical precision of the PyTorch implementation rather than exact analytical equality.

The convergence behavior for $x_c^* = (8, 12, 20)$ is further illustrated in Figure 3. Both the loss and the absolute error decrease steadily as the optimization proceeds. Moreover, initial guesses located farther from the true target typically require more iterations to reach convergence, while still recovering the correct location.

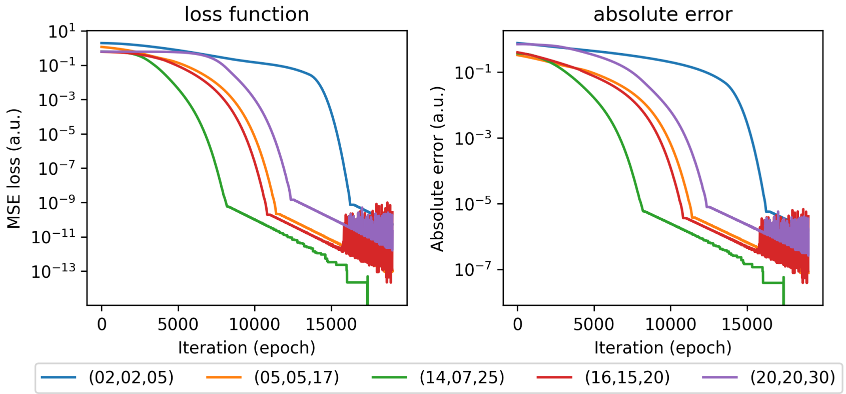

Figure 3. Convergence history for the single-target reconstruction with $x_c^* = (8, 12, 20)$. The figure shows the decay of the loss functional $\mathcal{L}$ and the absolute error $\|\hat{x}_c - x_c^*\|_2$ over optimization iterations for different initializations.

Figure 4 illustrates a representative optimization trajectory of the candidate point for the single-target case, where the true target is located at $x_c^* = (8, 12, 20)$ and the candidate is initialized at $(14, 7, 25)$. The trajectory projections onto the (x, y), (x, z), and (y, z) planes show that the candidate progresses smoothly toward the true target throughout the optimization process. In all coordinate projections, the motion follows a monotonic path without oscillatory or erratic behavior. Although the convergence rates differ across coordinates, the overall motion remains stable and is consistently guided by the gradient information induced by the full-waveform loss. This observation suggests that the proposed loss functional yields a well-shaped optimization landscape in the single-target setting, enabling reliable gradient-based convergence toward the correct spatial location.

Figure 5 shows the evolution of the predicted time-domain waveforms at several representative source–detector pairs during the optimization. At early iterations, noticeable discrepancies are observed not only in the overall amplitude but also in the temporal structure of the waveforms, including the timing of dominant features and the decay behavior. As the optimization proceeds, the predicted signals progressively align with the reference waveform over the entire time interval. In particular, the reconstruction simultaneously matches both the temporal alignment and the overall waveform shape, rather than fitting only reduced features such as the peak time. This convergence behavior is consistently observed across all examined S–D pairs, indicating that the reconstruction is driven by a global matching of the full temporal response and that the proposed method effectively exploits the complete time-domain information.

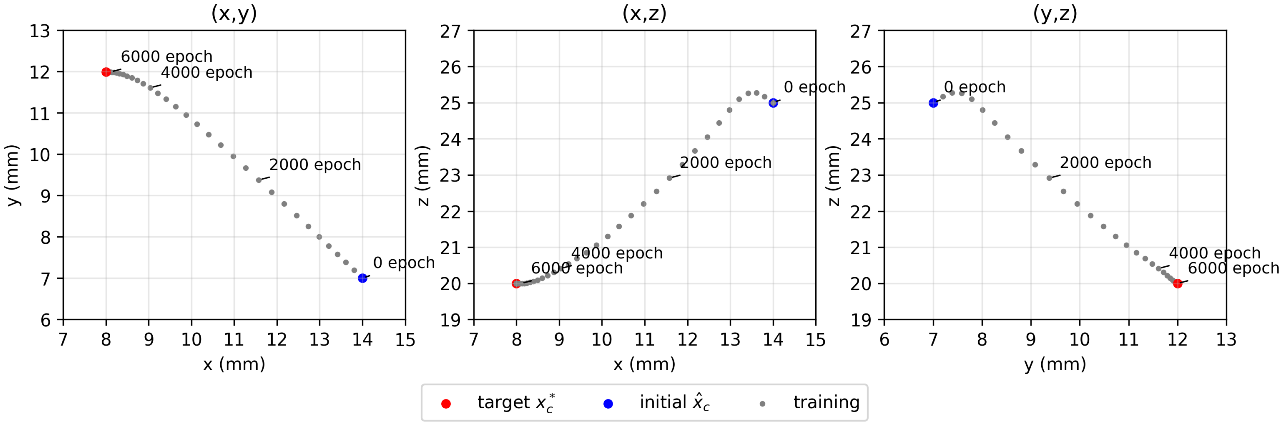

Figure 4. Trajectory of the candidate point for a representative single-target reconstruction. The true target is $x_c^* = (8, 12, 20)$, and the candidate point is initialized at $(14, 7, 25)$. The trajectory is shown as projections onto the (x, y), (x, z), and (y, z) planes.

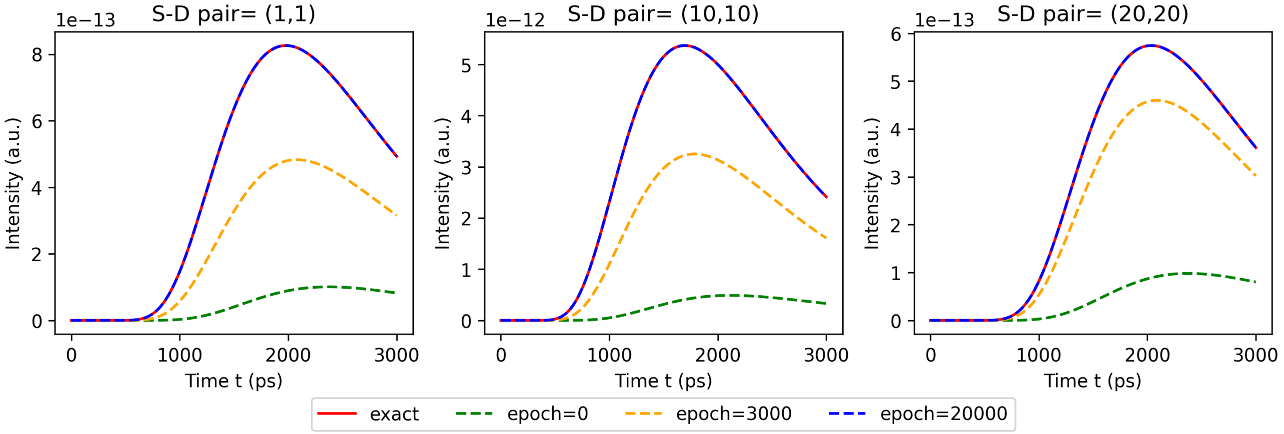

Figure 5. Evolution of predicted waveforms at representative S–D pairs during optimization (single-target case). The predicted waveforms at selected S–D indices approach the reference waveform as the candidate point converges to x_c^*.

In summary, the single-target experiments demonstrate that the proposed full-waveform reconstruction framework can reliably recover the location of a fluorescent point target with high numerical accuracy, independently of the initialization. The consistent convergence of the candidate point, together with the global matching of the temporal waveforms across all source–detector pairs, indicates that the time-domain data provide sufficient geometric information for stable localization in the single-target setting.

Having established the robustness and accuracy of the method for a single target, we next extend the reconstruction framework to configurations involving multiple fluorescence targets. In the multi-target case, the measured temporal response is given by a linear superposition of the individual target contributions, which leads to a more complex inverse problem. The following subsection examines whether the proposed full-waveform matching approach can still resolve multiple target locations simultaneously under this increased structural complexity.

5.2. Multiple-target reconstruction

Next we consider the reconstruction of multiple fluorescent point targets from time-domain FDOT data. In this setting, the reference waveform U_m^{exact} is generated by the linear superposition of the responses from multiple point targets, as described in Section 3. The inverse reconstruction is carried out using the same full-waveform matching framework introduced in Section 4, without any modification to the loss functional or the optimization procedure. As in the single-target experiments, the initial candidate locations are randomly sampled from the interior of the domain, without prior knowledge of the true target positions.

We first examine the case of two fluorescent point targets. Table 2 summarizes the reconstruction results for several two-target configurations, each tested with different random initializations of the candidate points. Despite the variability in the initial guesses, all candidates converge accurately to the true target locations, and stable convergence is consistently achieved within 20,000 training iterations.

Table 2. Reconstruction results for two-target configurations. For each target configuration x_c^*, the reconstruction is performed using two candidate points initialized at different random locations. The table reports the recovered target locations after 20,000 training iterations and the corresponding absolute reconstruction errors.

type	*Target*	*Initial*	*Prediction*	*Absolute Err*
2 points	(8, 8, 17) / (10, 10, 16)	(3, 2, 10) / (15, 16, 14)	(8.00001, 8.00001, 16.99999) / (10.00001, 10.00001, 16.00001)	3.75794e-05
		(5, 5, 20) / (6, 6, 19)	(7.99999, 7.99999, 17.00002) / (9.99999, 9.99999, 15.99999)	2.03303e-05
	(5, 5, 20) / (10, 10, 20)	(3, 2, 10) / (15, 16, 14)	(5.00001, 5.00001, 19.99998) / (10.00001, 10.00001, 20.00000)	2.70605e-05
		(9, 7, 14) / (11, 12, 13)	(5.00001, 5.00001, 19.99999) / (10.00001, 10.00001, 20.00000)	1.79018e-05
	(10, 10, 5) / (10, 10, 25)	(4, 3, 18) / (13, 17, 5)	(10.00000, 9.99999, 5.00000) / (10.00009, 9.99987, 24.99473)	2.63338e-03
		(5, 7, 10) / (16, 6, 19)	(10.00000, 10.00000, 5.00000) / (9.99985, 10.00013, 24.99494)	2.53203e-03

The tested configurations are designed to assess the robustness of the proposed method under different geometric arrangements. In addition to cases in which the two targets differ in all spatial coordinates, we also consider configurations where the targets share the same depth but are laterally separated, as well as a more challenging case in which the two targets have identical (x, y) coordinates and differ only along the depth direction. It is well known in fluorescence diffuse optical tomography that lateral localization in the (x, y) plane is generally more stable than depth localization along the z-axis due to the strong diffusive nature of light propagation and the limited depth sensitivity of boundary measurements. Accurately resolving target depth, therefore, remains a challenging aspect of time-domain FDOT, particularly when lateral information alone cannot disambiguate the target configuration in multi-target settings.

In this context, the configuration with targets located at $(10, 10, 5)$ and $(10, 10, 25)$ provides a stringent test for the reconstruction method as the two targets are perfectly aligned laterally and differ only along the depth direction. Despite this reduced geometric diversity, the proposed full-waveform matching approach successfully recovers both target locations with accuracy comparable to the other configurations. This result indicates that the temporal information contained in the full-waveform provides sufficient sensitivity to depth differences, even when the lateral positions coincide.

Overall, these results demonstrate that the proposed reconstruction framework reliably resolves multiple point targets across a range of geometric configurations, including depth separated cases that are known to be challenging in time-domain FDOT.

Next we extend the reconstruction to configurations involving three fluorescent point targets. The corresponding results are summarized in Table 3, where each experiment is performed with three candidate points initialized randomly within the domain. Compared to the two-target case, the three-target reconstruction problem introduces additional complexity due to the increased number of unknown target locations and stronger interactions among the superposed temporal responses. As a result, a larger number of training iterations is required to achieve convergence. Nevertheless, in all tested configurations, the proposed method successfully recovers all three target locations with high accuracy after approximately training iterations.

It is worth noting that the three targets are distributed both laterally and in depth, leading to distinct but partially overlapping temporal signatures in the measured data. The accurate reconstruction in this setting indicates that the full-waveform matching approach effectively exploits the global temporal structure of the signal to disentangle multiple contributions, even as the number of targets increases. Overall, the results in Table 3 demonstrate that the proposed reconstruction framework remains robust and scalable when applied to multi-target configurations with increased structural complexity.

Table 3. Reconstruction results for three-target configurations. For each configuration, three candidate points are initialized randomly and optimized using the full-waveform matching method. Accurate reconstruction of all targets is achieved after 40,000 training iterations.

Type	*Target*	*Initial*	*Prediction*	*Absolute Err*
3 points	(5, 5, 20) / (10, 10, 20) / (13, 13, 16)	(9, 7, 14) / (7, 8, 9) / (11, 12, 13)	(4.99995, 4.99995, 20.00006) / (10.00006, 10.00006, 20.00006) / (13.00006, 13.00006, 15.99993)	1.00966e-04
		(3, 4, 5) / (16, 7, 12) / (8, 13, 10)	(5.00000, 5.00000, 19.99999) / (9.99999, 9.99999, 19.99999) / (12.99999, 12.99999, 15.99999)	8.34870e-06

The convergence behavior of the multi-target reconstructions is illustrated in Figure 6. The left panel shows the decay of the loss functional for two representative two-target configurations with targets located at $(8, 8, 17)$ and $(10, 10, 16)$, whereas the right panel displays the loss histories for two representative three-target configurations with targets at $(5, 5, 20)$, $(10, 10, 20)$, and $(13, 13, 16)$. In all cases, the loss decreases steadily over the training iterations and reaches sufficiently small values, indicating successful convergence of the optimization. Compared with the two-target case, the three-target configurations require a larger number of iterations to converge, reflecting the increased number of unknown target locations and the more complex interactions among the superposed temporal responses. Nevertheless, the overall decay remains stable across different initializations, and no oscillatory or divergent behavior is observed.

Figure 7 further illustrates the reconstruction process for a representative two-target configuration by showing the trajectories of the candidate points in the three coordinate projections. Although the candidates are initialized at different locations and without any prior association to the true targets, each candidate is guided toward a distinct target location during the optimization. The trajectories exhibit smooth motion toward the corresponding targets, indicating that the full-waveform loss induces a well-structured optimization landscape that promotes stable spatial separation of the candidates.

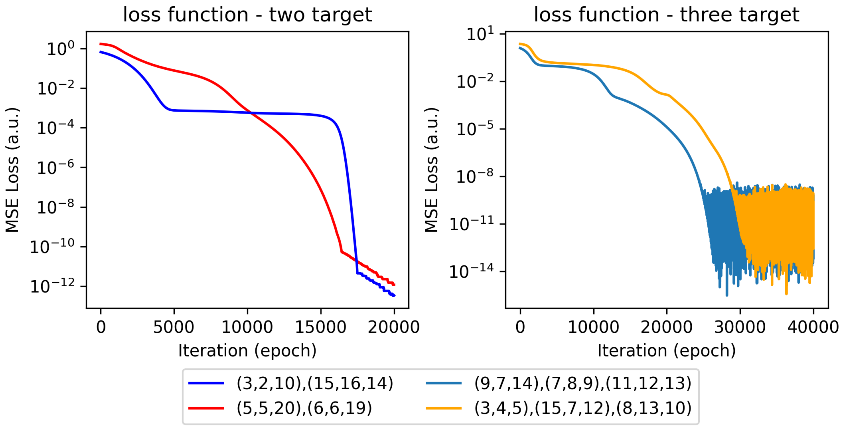

Figure 6. Convergence histories of the loss functional for multi-target reconstructions. The left panel shows representative two-target configurations, while the right panel displays representative three-target configurations with different random initializations of the candidate points.

Figure 7. Trajectories of the candidate points for a representative two-target reconstruction. Each candidate, initialized at a different location, is guided toward a distinct true target during the optimization, illustrating the natural separation of candidates induced by the full-waveform loss.

In this example, the candidate initialized at $(3, 2, 10)$ converges toward the target at $(5, 5, 20)$, while the candidate initialized at $(15, 16, 14)$ converges toward $(10, 10, 20)$. The trajectories exhibit smooth and stable motion toward the corresponding targets, without oscillatory or erratic behavior, indicating that the full-waveform loss induces a well-structured optimization landscape that promotes stable spatial separation of the candidates.

These observations naturally raise the question of how the proposed framework behaves when the number of candidate points exceeds the true number of targets, which motivates the overparameterized experiments in Section 5.3.

5.3. Reconstruction with an unknown number of targets

We finally consider a more challenging and practically relevant scenario in which the number of fluorescent targets is unknown a priori. In this setting, we assume that the reference waveform U_m^{exact} is available, but the number of point targets contributing to the measured signal is not provided.

To investigate this setting, we deliberately employ an overparameterized reconstruction model in which the number of candidate points exceeds the true number of targets. More precisely, although the data are generated from J point targets, the reconstruction is performed using K candidate locations with $K > J$. This setup mimics a realistic inverse problem in which only boundary measurements are available and the underlying target multiplicity is unknown.

In our numerical experiments, we consider a sequence of configurations with increasing numbers of true targets. Specifically, for data generated by a single target ($J = 1$), we perform reconstructions using three candidate points ($K = 3$). For data generated by two targets ($J = 2$), reconstructions are carried out using four and five candidate points ($K = 4$ and $K = 5$). Finally, for data generated by three targets ($J = 3$), we consider an overparameterized reconstruction with five candidate points ($K = 5$). In all cases, the candidates are initialized randomly within the domain, without prior knowledge of the true target locations, following the same strategy used in Sections 5.1 and 5.2. The objective of these experiments is to assess whether the proposed full-waveform matching framework can (i) identify the effective target structure encoded in the time-domain data and (ii) simultaneously suppress redundant candidate points introduced by overparameterization.

Table 4 summarizes representative results for overparameterized reconstructions in which the number of candidate points exceeds the true number of fluorescent targets. The experiments span configurations with one, two, and three true targets, allowing us to examine how the method behaves as the target multiplicity increases.

For $J = 1$, three candidates ($K = 3$) are used to reconstruct data generated by a single target. Although all candidates are initialized without prior information and evolve freely during optimization, only one candidate converges accurately to the true target location. The remaining candidates migrate toward locations whose contributions to the predicted signal are negligible, indicating that redundant degrees of freedom are naturally suppressed. A similar behavior is observed for $J = 2$. When the data are generated by two targets, reconstructions with $K = 4$ and $K = 5$ candidates consistently recover the two true target locations, while the remaining candidates do not exhibit meaningful convergence. Despite the increased dimensionality of the optimization problem, the recovered target positions remain accurate. The suppression mechanism persists for $J = 3$. Even when three targets are present and five candidates ($K = 5$) are used, the optimization identifies three effective candidates that converge to the true target locations. The additional candidates are automatically suppressed and contribute negligibly to the reconstructed waveform, demonstrating robustness as the number of targets increases.

Table 4. Reconstruction results for overparameterized settings with $J < K$. The table reports representative results for configurations with one, two, and three true fluorescence targets reconstructed using a larger number of candidate points. Bold entries indicate candidate locations that converge to the true target positions, while non-bold entries correspond to redundant candidates whose contributions to the predicted waveform become negligible during optimization.

type	*Target*	*Initial*	*Prediction*	*Absolute Err*
J=1, K=3	(8, 12, 16)	(4, 4, 8) / (10, 10, 10) / (14, 14, 14)	(6.18499, 12.67402, 37.08894) / **(8.00008, 12.00009, 15.99995)** / (11.59888, 10.27413, 38.17801)	1.32729e-04
J=2, K=4	(5, 5, 20) / (10, 10, 16)	(8, 8, 14) / (7, 7, 13) / (9, 9, 12) / (6, 6, 12)	(5.55620, 6.43104, 38.36529) / **(4.99977, 4.99976, 20.00019)** / **(9.99996, 9.99995, 15.99999)** / (11.16529, 10.74556, 37.00825)	3.79365e-04 / 5.71728e-05
J=2, K=5	(5, 5, 20) / (10, 10, 16)	(4, 5, 17) / (8, 6, 15) / (9, 11, 12) / (12, 13, 14) / (14, 7, 10)	(4.68120, 6.32308, 37.95543) / **(4.99977, 4.99961, 20.00037)** / (9.02715, 9.02113, 36.50741) / (13.75349, 12.53287, 37.68816) / **(9.99991, 9.99993, 15.99998)**	5.85752e-04 / 1.05514e-04
J=3, K=5	(5, 5, 20) / (10, 10, 16) / (13,13,25)	(4, 5, 17) / (8, 6, 15) / (9, 11, 12) / (12, 13, 14) / (14, 7, 10)	(0.00000, 0.00000, 37.48822) / **(5.00053, 5.00054, 19.99970)** / **(12.99235, 12.99220, 24.99752)** / (17.54517, 17.55571, 40.62462) / **(9.99998, 9.99998, 16.00004)**	8.20351e-04 / 1.11971e-02/ 5.58368e-05

The convergence behavior of the overparameterized reconstructions is further illustrated in Figure 8. Across all tested configurations, the loss functional decreases by several orders of magnitude, indicating that the predicted waveforms progressively approach the reference data. Compared to cases in which the number of candidates matches the number of true targets, the overparameterized settings generally require more iterations to reach convergence. This behavior is expected, as the optimization involves a higher-dimensional parameter space and additional degrees of freedom. Nevertheless, the loss decay remains smooth and stable throughout training, and no oscillatory or divergent behavior is observed.

Importantly, the observed reduction of the loss does not rely on any explicit constraint that enforces equal contributions from all candidate points. Recall that the predicted signal is given by a superposition of individual waveform components u_m, as defined in (2.1). As shown in the right panel of Figure 8, which reports the L^2 norms of the individual components, only the components associated with candidates converging toward the true target locations retain non-negligible magnitudes, while the remaining components are progressively suppressed. This indicates that the full-waveform loss provides sufficient discriminative information to guide the optimization, even in the presence of redundant candidates. The numerical diagnostics presented in Figure 9 further elucidate this mechanism; while the λ values of candidates converging to target A, B, and C remain stable at their true levels, those of the redundant candidates continue to rise throughout the iterations. This ensures that the waveforms associated with spurious points are naturally filtered out of the reconstruction process without requiring any explicit pruning strategy.

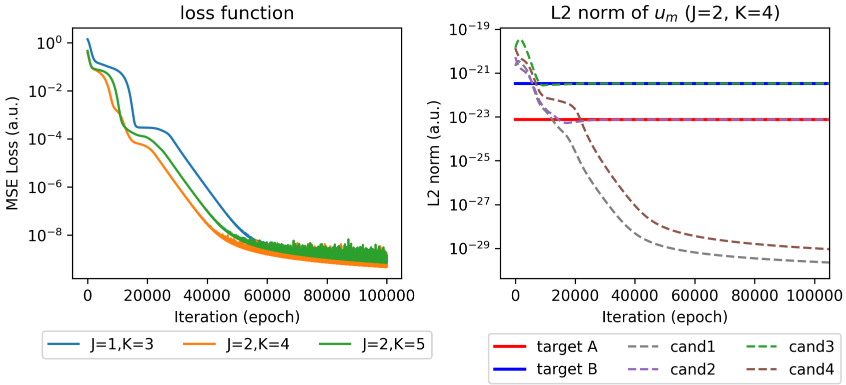

Figure 8. Convergence behavior for overparameterized reconstructions with different combinations of (J, K). (Left): Histories of the loss functional for the cases $J = 1$, $K = 3$, $J = 2$, $K = 4$, and $J = 2$, $K = 5$, showing stable decay despite the presence of redundant candidate points. (Right): Evolution of the L^2 norms of the individual waveform components u_m for the case $J = 2$ and $K = 4$, with true targets located at target A $(5, 5, 20)$ and target B $(10, 10, 16)$. The four candidates are initialized at $(8, 8, 14)$, $(7, 7, 13)$, $(9, 9, 12)$, and $(6, 6, 12)$. Only two candidates maintain non-negligible waveform magnitudes and align with the true targets, while the remaining candidates are automatically suppressed during the optimization.

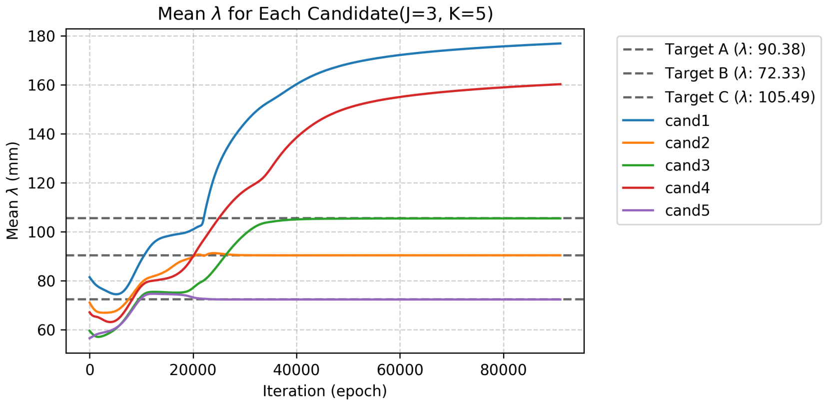

Figure 9. Trajectories of the average of distance parameter λ during the optimization process for $J = 3$ and $K = 5$. The horizontal dashed lines indicate the true λ values for target A(5, 5, 20), B(10, 10, 16), and C(13, 13, 25). Candidates 2(8, 6, 15), 3(9, 11, 12), and 5(14, 7, 10) converge to these true levels, whereas the redundant candidates (cand1(4, 5, 17) and cand4(12, 13, 14)) exhibit a steady increase in λ. This migration toward larger distances provides the numerical basis for the exponential decay of their signal contributions, as predicted by Lemma 2.1.

Figure 10 shows the trajectories of the three candidate points for the overparameterized case $J = 1$ and $K = 3$ in the (x, y), (x, z), and (y, z) projections. Although all candidates are initialized away from the true target and treated symmetrically, only one candidate is guided to the correct location. The remaining candidates follow distinct trajectories and gradually move toward regions where their influence on the measured signal becomes negligible. Notably, the effective candidate exhibits a consistent attraction toward the true target across all projections, whereas the redundant candidates diverge from the target point. In particular, the z-coordinates of the redundant candidates increase steadily during the optimization. As shown in Figure 9, this spatial migration directly corresponds to a monotonic increase in the distance parameter λ for the redundant candidates (cand1 and cand4). By the asymptotic estimate in Lemma 2.1, such an increase in λ implies that the associated waveform contributions u_m decay to zero (Figure 11). This spatial behavior is consistent with the signal-level suppression observed in Figure 8, indicating that the full-waveform loss promotes separation between relevant and redundant candidates in both physical space and waveform space.

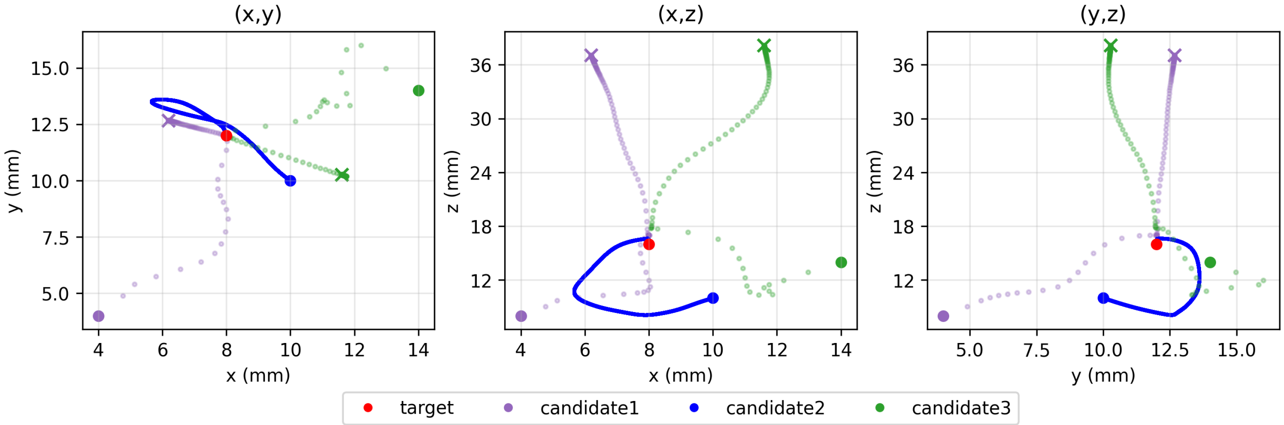

Figure 10. Trajectories of the candidate points for the overparameterized case $J = 1$ and $K = 3$, shown in the (x, y), (x, z), and (y, z) coordinate projections. Although all candidates are initialized away from the true target, only one candidate is guided toward the correct location, while the remaining candidates follow distinct trajectories and migrate toward regions with negligible influence on the measured signal.

To further elucidate the mechanism underlying the suppression of redundant candidates, we examine the individual contributions of each candidate point to the zero-lifetime signal u_m in the forward model. Recall that the predicted signal is constructed by the superposition in (4.1), where each candidate location independently enters the integral representation in (2.1). Figure 11 shows the evolution of the waveform components associated with the three candidates for $J = 1$ and $K = 3$ at several representative training epochs. At early iterations, all candidates produce waveform contributions of comparable magnitude, indicating that the optimization initially explores multiple explanations of the measured data. As training progresses, the waveform corresponding to the candidate converging toward the true target aligns with the temporal profile of the reference signal.

In contrast, the waveform components associated with the remaining candidates decay rapidly and become negligible. This decay is not imposed by any explicit regularization or sparsity constraint, but arises naturally from the full-waveform matching objective. As a result, only candidates that are geometrically consistent with the true targets continue to contribute to the predicted signal, while redundant candidates are automatically suppressed. Together with the trajectory analysis in Figure 10 and the L^2-norm behavior in Figure 8, these results show that the proposed framework achieves coherent candidate selection in both physical space and waveform space.

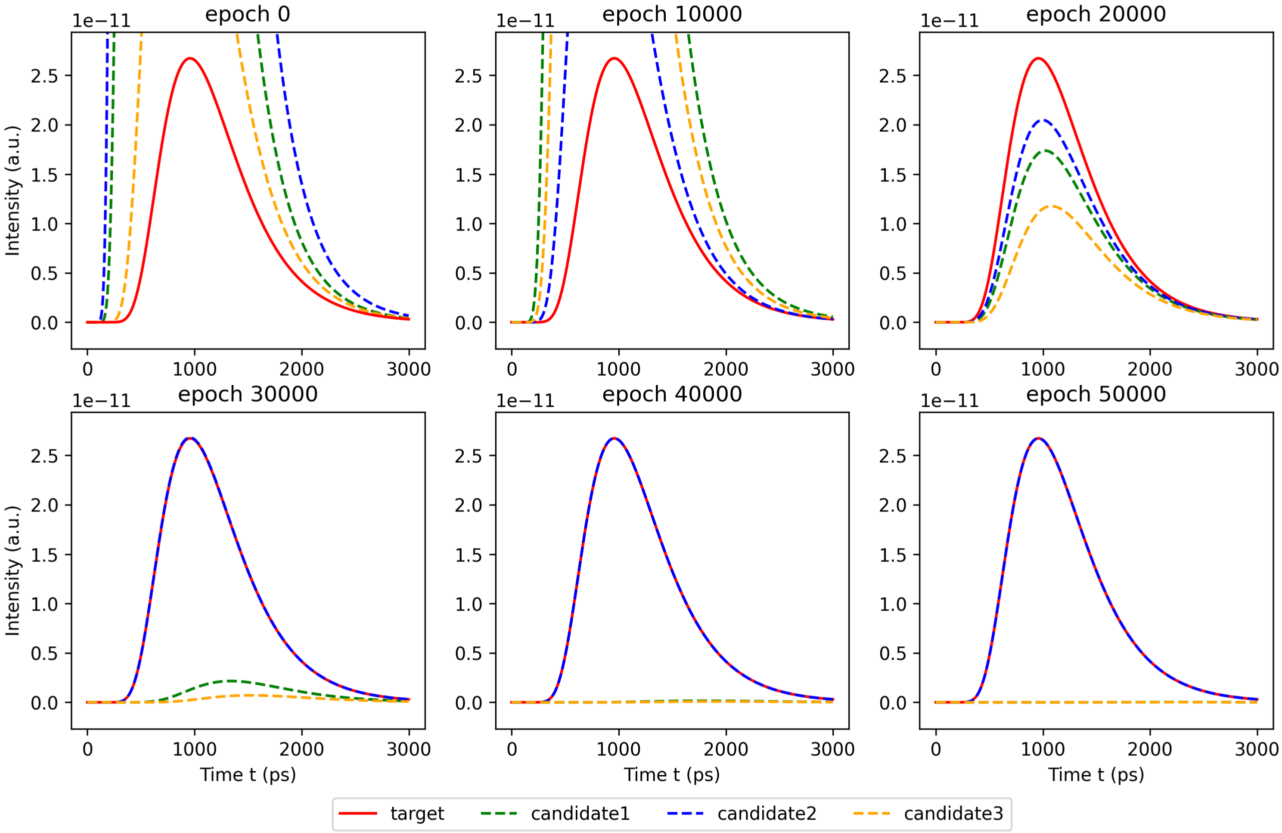

Figure 11. Evolution of individual waveform contributions of the candidate points for the overparameterized case $J = 1$ and $K = 3$. Each panel shows the predicted zero-lifetime signal $u_m(t)$ associated with a single candidate point at different training epochs. At early iterations, all candidates produce non-negligible waveform contributions. As the optimization proceeds, only the candidate converging toward the true target maintains a waveform that matches the reference signal, while the contributions from the remaining candidates are progressively suppressed and become negligible.

In summary, the experiments demonstrate that the proposed full-waveform reconstruction framework can handle inverse FDOT problems when the number of fluorescent targets is unknown in advance. Across configurations with increasing target multiplicity, the method identifies the effective target structure encoded in the time-domain data while automatically suppressing redundant candidates introduced by overparameterization. Importantly, this behavior emerges without explicit sparsity constraints, regularization terms, or pruning strategies. Instead, relevant candidates are selected implicitly through the full-waveform matching objective, which enforces consistency at both the signal and spatial levels. These results highlight a key advantage of the proposed approach for practical FDOT applications, where prior information on target multiplicity is unavailable.

5.4. *Robustness analysis*

The results presented so far demonstrate the effectiveness of the proposed framework under idealized, noise-free conditions. In practical FDOT applications, however, various sources of uncertainty are unavoidable. In realistic settings, measurement data are inevitably corrupted by various noise sources, and the optical properties of the background medium, such as the absorption (μ_a) and diffusion (D) coefficients, are often not known with perfect precision. To rigorously evaluate the reliability and practical applicability of our method, we conduct a comprehensive robustness analysis.

All experiments in this subsection are conducted under an overparameterized setting ($J < K$), which represents a realistic scenario where the exact number of targets is unknown a priori. To address the potential sensitivity to initial candidate locations, we adopt a spatially-stratified (layered) random initialization strategy. Specifically, we partition the domain into K distinct layers along the depth (z-axis) and randomly initialize each candidate point within its assigned layer. This strategy ensures broad spatial coverage and prevents numerical stagnation near shallow local minima, which is particularly vital given the diffusive and exponentially decaying nature of the fluorescence signal in deep tissue.

In the following subsections, we evaluate the robustness of our framework using a representative multi-target configuration, where targets are distributed at diverse spatial coordinates. We examine the algorithm's performance under increasing levels of measurement noise and systematic mismatches in optical properties.

5.4.1. Measurement noise

In this subsection, we examine the performance of the proposed reconstruction framework when the measured fluorescence signals are contaminated by additive white Gaussian noise. To evaluate the robustness in a multi-target scenario, we consider a representative configuration consisting of three point targets located at (5, 5, 20), (10, 10, 16), and (13, 13, 25). These coordinates are chosen to represent a non-symmetric distribution within the domain.

To simulate realistic experimental conditions, we apply noise levels of 1%, 3%, and 5% (relative RMS) to the synthetic temporal data. All reconstructions are performed under the overparameterized setting with $K = 5$ candidate points, using the spatially-stratified random initialization described above.

Table 5 summarizes the final reconstructed target locations under different noise levels. For all tested cases, the proposed framework successfully identifies the three true target locations, even when the measured signals are subject to significant oscillations induced by 5% RMS noise.

As expected, the absolute localization errors tend to increase as the noise level rises. For instance, at a 1% noise level, the absolute errors are typically on the order of 10^{-3} to 10^{-2} mm, indicating nearly perfect recovery. Even at a 5% noise level, which represents a highly challenging measurement condition, the maximum absolute error remains below 0.7 mm, demonstrating the inherent robustness of the full-waveform matching objective. Notably, the depth (z) coordinates show slightly larger deviations compared to the lateral (x, y) coordinates under high noise. This is consistent with the diffusive nature of light propagation, where the broadening of the temporal point spread function (TPSF) at greater depths leads to a inherent reduction in depth-wise resolution.

Table 5. Final reconstructed target locations for measurement data corrupted by varying levels of additive Gaussian noise (1%, 3%, and 5%). Reconstructions are performed in an overparameterized setting ($J = 3, K = 5$) using a spatially-stratified random initialization. Bold entries indicate the candidate locations that accurately converge to the true target positions, while the remaining candidates are suppressed and migrate toward the boundaries.

noise	*Target*	*Initial*	*Prediction*	*Absolute Err*
1%	(5, 5, 20) / (10, 10, 16) / (13, 13, 25)	(6.52, 19.93, 3.28) /	(5.79524, 6.21979, 34.57796)/	
		(5.78, 10.07, 8.56) /	**(9.99944, 9.99910, 15.99911)** /	1.37102e-03 /
		(11.51, 16.62, 14.68) /	(11.80565, 11.58155, 32.95815) /	
		(2.39, 5.48, 20.18) /	**(4.99289, 4.99401, 20.00418)** /	1.01927e-02 /
		(19.62, 3.63, 25.22)	**(12.98950, 13.01491, 25.02044)**	2.73948e-02
3%	(5, 5, 20) / (10, 10, 16) / (13, 13, 25)	(2.22, 10.53, 4.11) /	**(13.16748, 13.01644, 25.04795)** /	1.74990e-01 /
		(12.23, 1.06, 8.13) /	**(9.99768, 9.99900, 16.00994)** /	1.02593e-02/
		(8.06, 14.60, 15.40) /	(1.26928, 34.47249, 29.39052) /	
		(16.51, 6.41, 19.87) /	**(4.98117, 4.98081, 20.02017)** /	3.36100e-01
		(7.22, 18.24, 24.40)	(12.26878, 0.00000, 38.03949)	
5%	(5, 5, 20) / (10, 10, 16) / (13, 13, 25)	(1.88, 0.66, 6.51) /	**(13.51189, 13.36572, 25.27195)** /	6.85389e-01 /
		(10.43, 16.63, 10.02) /	(0.00000, 44.33101, 11.53893) /	
		(7.77, 8.25, 13.19) /	**(9.99308, 9.99258, 16.06471)** /	1.51422e-01/
		(1.05, 16.27, 21.62) /	**(4.92330, 4.93504, 20.11325)** /	6.55038e-02
		(6.97, 9.30, 26.92)	(0.00000, 0.00000, 39.35872)	

Furthermore, the overparameterization mechanism remains effective in the presence of noise. Although $K = 5$ candidates were employed for $J = 3$ targets, only the three relevant candidates converged toward the true locations. The redundant candidates moved toward the domain boundaries or regions with negligible sensitivity (e.g., $z > 30$). As established in Lemma 2.1, this migration to larger depths leads to an exponential decay of their signal contributions, ensuring that they do not interfere with the fitting of the reference data. This behavior confirms that our asymptotic suppression strategy does not lead to over-fitting of the stochastic noise components, but instead naturally isolates the effective target structure from the corrupted measurements.

To illustrate the effect of measurement noise on the time-domain signal, we examine a representative temporal waveform obtained from a single source–detector (S–D) pair. Figure 12 compares the noise-free reference waveform $U_m^{\text{exact}}(t)$ and its noisy counterpart $U_m^{\text{noise}}(t)$ at the center S–D pair $(m, n) = (10, 10)$.

As shown in Figure 12, the addition of 5% RMS Gaussian noise introduces high-frequency oscillations throughout the entire temporal response. Nevertheless, the global structure of the waveform,including the rise time, peak amplitude, and decay behavior,remains clearly discernible. This observation indicates that although the noise perturbs the fine-scale structure of the signal, the dominant temporal features that encode the geometric information of the fluorophores are largely preserved. By minimizing the discrepancy over the entire temporal profile, the proposed framework effectively averages out high-frequency stochastic noise while prioritizing these robust geometric signatures, enabling stable localization even under significantly corrupted measurements.

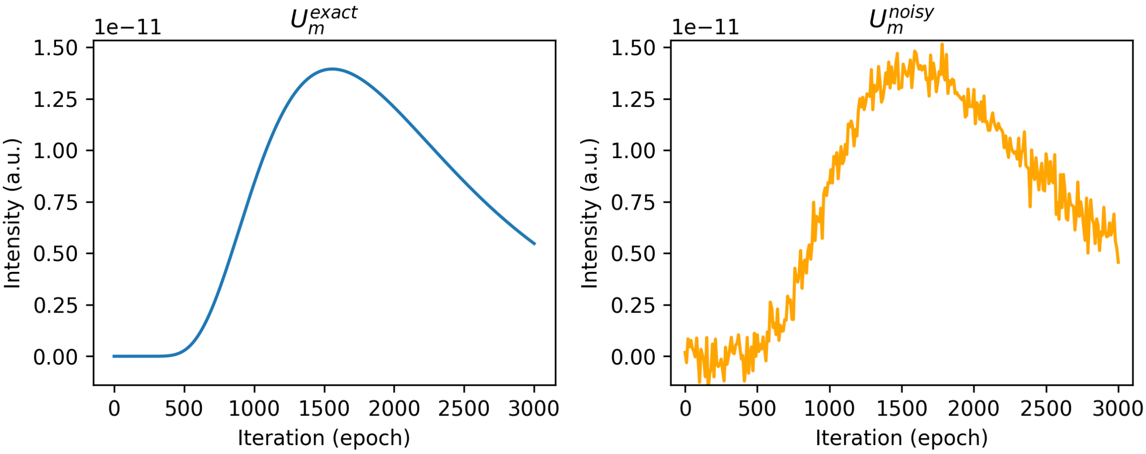

Figure 12. Comparison of the noise-free waveform $U_m^{\text{exact}}(t)$ and the noisy waveform $U_m^{\text{noise}}(t)$ for the S–D pair $(m, n) = (10, 10)$. The noisy signal exhibits noticeable oscillations induced by additive Gaussian noise with a 5% RMS noise level, while preserving the overall temporal structure of the waveform.

5.4.2. Impact of optical property mismatch

In practical FDOT applications, the optical properties of the background medium, specifically the absorption coefficient (μ_a) and the diffusion coefficient (D), are often estimated with some degree of uncertainty. To evaluate the resilience of our framework against such model mismatches, we perform reconstructions using perturbed background properties. We introduce systematic errors of 1%, 3%, and 5% to the ground truth values of μ_a and D, respectively, while maintaining the same target configuration as in the previous subsection.

Table 6 summarizes the reconstruction results under mismatches in μ_a. The framework accurately identifies the locations of all three targets even with a 5% deviation in the absorption coefficient. While the absolute localization error increases slightly as the mismatch level rises, particularly for the deepest target (target C), the recovered positions remain within a sub-millimeter range. This stability suggests that the full-waveform matching objective is inherently robust to small scaling errors in absorption, as the temporal peak structures remain largely consistent.

Similarly, Table 7 presents the performance under mismatches in the diffusion coefficient D. Since D directly governs the diffusive broadening and the arrival time of the fluorescence pulse, its mismatch exhibits a more pronounced impact on the localization accuracy compared to μ_a. At a 5% mismatch level, the errors for the deepest target show larger deviations. Nevertheless, the three relevant candidates consistently align with the true target locations, demonstrating the algorithm's capacity to handle uncertainties in scattering properties.

Importantly, the suppression mechanism for redundant candidates remains effective even under systematic model mismatch. Despite the perturbations in μ_a or D, the redundant candidates do not "over-fit" the erroneous background parameters. Instead, they migrate toward larger depths where the distance parameter λ increases, causing their waveform contributions to vanish as predicted by the asymptotic behavior in Lemma 2.1. These results highlight the practical feasibility of the proposed method, as it maintains reliable performance without requiring perfectly calibrated optical properties.

Table 6. Final reconstructed target locations under systematic mismatches in the absorption coefficient μ_a. The synthetic data were generated with the baseline μ_a, while the reconstructions were performed using mismatched values shifted by 1%, 3%, and 5%, respectively. Reconstructions employ an overparameterized setting ($J = 3, K = 5$) with spatially-stratified random initialization. Bold entries indicate successful convergence to the true targets.

noise	*Target*	*Initial*	*Prediction*	*Absolute Err*
1%		(6.90, 0.67, 3.63) /	**(11.92612, 11.91595, 24.32796)** /	1.66733e+00 /
	(5, 5, 20) /	(5.93, 17.16, 11.67) /	**(10.00315, 10.00284, 15.99089)** /	1.00496e-02 /
	(10, 10, 16) /	(0.50, 7.43, 16.02) /	**(5.04202, 5.04954, 19.95460)** /	7.92583e-02
	(13, 13, 25)	(3.61, 19.65, 19.11) /	(17.96685, 17.69108, 30.44871) /	
		(7.19, 13.65, 26.31)	(0.60777, 0.27994, 30.53446)	
3%		(6.76, 13.47, 5.64) /	**(10.00149, 10.00155, 15.97192)** /	2.81561e-02 /
	(5, 5, 20) /	(7.32, 1.13, 10.12) /	**(5.03210, 5.03148, 19.94582)** /	7.04076e-02/
	(10, 10, 16) /	(7.94, 10.38, 13.06) /	(11.11966, 11.10155, 23.62845) /	
	(13, 13, 25)	(1.92, 18.19, 18.97) /	**(14.29053, 13.88207, 26.88898)** /	2.45190+00
		(6.10, 13.02, 24.16)	(5.60169, 5.98692, 26.43174)	
5%		(11.06, 16.95, 6.80) /	(10.07527, 10.08468, 21.92679) /	
	(5, 5, 20) /	(10.32, 16.47, 8.41) /	**(5.00416, 5.01098, 19.91444)** /	8.63626e-02/
	(10, 10, 16) /	(12.97, 6.25, 13.96) /	**(10.00247, 10.00247, 15.95378)** /	4.63637e-02 /
	(13, 13, 25)	(3.23, 1.83, 19.89) /	**(14.41346, 13.94019, 25.77639)** /	1.86672e+00
		(1.41, 12.87, 23.25)	(4.29581, 4.73987, 26.15159)	

Table 7. Final reconstructed target locations under systematic mismatches in the diffusion coefficient D. The predicted locations were obtained by assuming mismatched D values (1%, 3%, and 5% deviation from the true value). Bold entries denote candidates that accurately localized the targets, demonstrating the robustness of the full-waveform matching objective against uncertainties in the scattering properties of the medium.

noise	*Target*	*Initial*	*Prediction*	*Absolute Err*
1%		(15.38, 17.25, 5.47) /	**(15.27224, 15.23770, 25.92807)** /	6.16177e-02 /
	(5, 5, 20) /	(4.81, 17.35, 10.73) /	**(9.99230, 9.99229, 16.06064)** /	2.67499e-01 /
	(10, 10, 16) /	(9.37, 8.04, 13.16) /	(0.00000, 23.59194, 29.32498) /	
	(13, 13, 25)	(17.26, 16.67, 20.83) /	**(4.85141, 4.85187, 20.16594)** /	3.32141e+00
		(4.14, 4.93, 23.61)	(23.21504, 0.00000, 29.36840)	
3%		(14.97, 9.01, 6.37) /	**(9.97977, 9.97940, 16.18078)** /	1.83073e-01 /
	(5, 5, 20) /	(12.75, 6.92, 10.03) /	**(18.67717, 18.50920, 25.98020)** /	7.97135e+00/
	(10, 10, 16) /	(2.07, 11.34, 16.02) /	(25.34831, 0.00000, 26.42570) /	
	(13, 13, 25)	(4.64, 0.73, 18.95) /	(0.00000, 25.95032, 26.33644) /	
		(8.49, 19.79, 25.91)	**(4.54589, 4.55478, 20.44433)**	7.75793e-01
5%		(1.85, 4.86, 5.08) /	**(9.96882, 9.96736, 16.29695)** /	3.00366-01 /
	(5, 5, 20) /	(7.35, 12.68, 9.28) /	**(4.47576, 4.52361, 20.72495)** /	1.01357e+00/
	(10, 10, 16) /	(9.17, 17.10, 14.84) /	(34.26580, 0.00000, 23.83225) /	
	(13, 13, 25)	(14.23, 18.28, 21.08) /	**(18.06337, 20.10458, 26.77555)** /	2.10881e+01
		(15.19, 0.17, 26.70)	(0.00000, 0.00000, 40.38137)	

5.5. Reconstruction of extended ball target

To further demonstrate the versatility and practical applicability of the proposed framework, we extend our evaluation to the reconstruction of extended spherical (ball) targets. In real-world diagnostic scenarios, fluorophore distributions, such as those within solid tumors, occupy a finite volume rather than being concentrated at idealized points. Therefore, it is essential to verify whether the point-based optimization strategy can accurately localize the centers and estimate the volumes of these extended inclusions.

In this experiment, we define a spherical target with a radius of $R = 1.0$ mm centered at $(8.0, 12.0, 20.0)$ mm. To compute the forward response of the ball target, we utilized a deterministic Gauss–Legendre sampling scheme ($N_r = 3, N_\theta = 4, N_\phi = 6$). This allowed for the efficient numerical integration of the fluorescence density over the spherical volume within the causality-aware training loop. Unlike the previous robustness tests, the radius r is treated as an additional optimizable parameter. The gradients from the causality-aware loss function are backpropagated not only to the centroid coordinates, but also to the radius, enabling the simultaneous recovery of the target's size and location.

Table 8 summarizes the results. The candidate point, initially placed at $(4.0, 3.0, 18.0)$, effectively converged to the true centroid with an absolute position error of 9.425×10^{-2}. Furthermore, the radius r converged from its initial value of 0.6381 mm to 0.98837, yielding a remarkably low error of 1.163×10^{-2}.

Table 8. Reconstruction results for an extended spherical (ball) target. The target is defined by its centroid coordinates and radius r. The absolute error is reported separately for the centroid position and the radius, demonstrating the framework's capability to recover both the location and the volume of the inclusion.

Type	*Target*	*Initial*	*Prediction*	*Absolute Err*
Single Ball	(8, 12, 20) / r=1	(4.0, 3.0, 18.0) / r=0.6381	(7.96841, 12.01339, 19.91121) / r=0.98837	9.42512e-02 / 1.16300e-02

The success of this volumetric reconstruction indicates that our point-based framework can be naturally extended to more complex, non-stationary geometries. By representing a large inclusion as a collection of trainable spheres or points, the proposed method bypasses the need for computationally expensive high-resolution voxel grids. This demonstrates the potential of our approach for real-time practical applications, such as intraoperative tumor margin assessment, where both rapid localization and size estimation are paramount.

6. Conclusions

In this work, we proposed a full-waveform reconstruction framework for time-domain fluorescence diffuse optical tomography (FDOT) to localize multiple fluorescent point targets from boundary measurements. In contrast to approaches based on reduced temporal features such as peak time [11–13] or temporal moments [14–16], the proposed method leverages the entire time-resolved fluorescence waveform, thereby exploiting richer geometric and temporal information in the inverse reconstruction.

A notable advantage of the full-waveform formulation is its sensitivity to depth information. While depth localization in FDOT is widely considered challenging compared with lateral localization, our results indicate that the temporal waveform contains sufficient information to discriminate targets that differ only in depth, even in multi-target and overparameterized reconstructions. The robustness of this approach was further validated through comprehensive sensitivity analyses. Our results confirm that the framework maintains stable reconstruction performance even under significant measurement noise (up to 5% RMS) and systematic mismatches in background optical properties, such as the absorption

(μ_a) and diffusion (D) coefficients. These findings underscore the practical feasibility of the method in environments where perfectly calibrated model parameters are unavailable.

The ability to reconstruct targets without prior knowledge of their number further enhances the practical relevance of the proposed approach. Furthermore, the successful reconstruction of extended spherical targets in Section 5.5 demonstrates that the point-based optimization strategy can be effectively generalized to volumetric inclusions. By accurately recovering both the centroid and the radius of the ball targets, the proposed method shows its potential for handling more realistic, non-point-like fluorophore distributions.

By exploiting the global temporal structure of time-domain measurements, the method provides a unified reconstruction strategy that remains effective under varying model complexity. Although this study primarily focuses on point-target and spherical configurations, the results provide a strong foundation for handling arbitrary continuous distributions. Future work will extend the framework by adopting physics-informed neural networks (PINNs) and operator learning approaches for inverse problems [18, 19], as well as integrating advanced geometric representations such as level sets or implicit neural representations to resolve heterogeneous tumor morphologies. Moreover, incorporating more realistic noise models and validating the approach using experimental or in vivo datasets are important directions for future investigation.

A. Appendix

In this appendix, we provide a proof of Lemma 2.1 in non-dimensional form. To treat all parameters appearing in the solution u_m in (2.1) in a dimensionless setting, we introduce the following non-dimensional length and time variables:

$$\rho = \frac{x}{D},\ \rho_d = \frac{x_d}{D},\ \rho_s = \frac{x_s}{D},\ \rho_c = \frac{x_c}{D},\ \tau = \frac{vt}{D},\ b = \beta D,$$

and

$$\tilde{u}_m(\rho, \tau; \rho_s) := u_m(x, t; x_s), \quad \tilde{\mathcal{K}}_3(\rho_3; \tau) := \hat{\mathcal{K}}_3(x_{c_3}; t).$$

Then, $\tilde{u}_m$ is written as follows (see [17, Lemma 2.1]).

Lemma A.1. *For any given* $\rho_d,\ \rho_s \in \partial\Omega$,

$$\tilde{u}_m(\tau) = C(\tau)\tau^{-2}(I_{\lambda_{d,s}}(\tau) + I_{\lambda_{s,d}}(\tau)), \tag{A.1}$$

where

$$C(\tau) := \frac{cv\exp(-\mu_a D\tau)}{16\pi^3 D^4},\ \lambda_d := \frac{|\rho_d - \rho_c|^2}{4\tau},\ \lambda_s := \frac{|\rho_s - \rho_c|^2}{4\tau},\ \lambda_c := \frac{\rho_{c_3}^2}{4\tau}, \tag{A.2}$$

$$I_{\lambda_{d,s}}(\tau) := \int_0^{1/2} ((1-\sigma)\sigma)^{-\frac{3}{2}} e^{-\frac{\lambda_d}{(1-\sigma)\sigma}} e^{-\frac{\lambda_s - \lambda_d}{1-\sigma}} \tilde{\mathcal{K}}_3(\lambda_c; 1-\sigma)\tilde{\mathcal{K}}_3(\lambda_c; \sigma)\, \mathrm{d}\sigma, \tag{A.3}$$

and $I_{\lambda_{s,d}}(\tau)$ *is defined by switching the role of* λ_d *and* λ_s *in* $I_{\lambda_{d,s}}(\tau)$. *Here,* $\tilde{\mathcal{K}}_3$ *is given as*

$$\tilde{\mathcal{K}}_3(\lambda_c; \sigma) = 1 - \frac{b\sqrt{\tau\sigma}}{\sqrt{\lambda_c} + b\sqrt{\tau\sigma}} \sqrt{\pi}\, z_\sigma \exp\left(z_\sigma^2\right) \operatorname{erfc}(z_\sigma) \tag{A.4}$$

with $z_\sigma = \frac{\sqrt{\lambda_c} + b\sqrt{\tau\sigma}}{\sqrt{\sigma}}$ *for* $0 < \sigma < 1$.

In Theorem 7.2, we obtain the asymptotic behavior of $\tilde{u}_m$ based on the asymptotic of $\tilde{\mathcal{K}}_3$ as $\rho_{c_3} \to \infty$, where $\rho_{c_3} > 0$ is the depth component of $\rho_c > 0$.

Theorem A.2. *Let* $\rho_d,\ \rho_s \in \partial\Omega$. *Assume that*

$$\left| |\rho_d - \rho_c|^2 - |\rho_s - \rho_c|^2 \right| \le C\tau \quad \textit{for some} \quad C > 0. \tag{A.5}$$

Then, $\tilde{u}_m$ *of* (A.1) *satisfies*

$$\tilde{u}_m(\tau) = \tilde{u}_m^a(\tau) + O\left(\tilde{u}_m^a(\tau)\rho_{c_3}^{-1}\right) \tag{A.6}$$

as $\rho_{c_3} \to \infty$, *where*

$$\tilde{u}_m^a(\tau) := \sqrt{\pi}C(\tau)\tau^{-\frac{3}{2}}\left(\frac{2}{|\rho_d - \rho_c|} + \frac{2}{|\rho_s - \rho_c|}\right)e^{-\frac{|\rho_d-\rho_c|^2+|\rho_s-\rho_c|^2}{2\tau}}\left(\frac{\rho_{c3}}{\rho_{c_3} + b\tau}\right)^2. \tag{A.7}$$

Proof. The proof of Theorem 7.2 can be done in a similar way as in [17, Corollary 2.3]. For readers' convenience, we provide the proof here in detail. By (A.4) and

$$\begin{aligned}\exp\left(z^2\right)\operatorname{erfc}(z) &= \frac{2}{\sqrt{\pi}}\exp\left(z^2\right)\int_z^\infty \exp\left(-s^2\right)\mathrm{d}s\\ &= \frac{1}{\sqrt{\pi}z} - \frac{\exp\left(z^2\right)}{\sqrt{\pi}}\int_z^\infty s^{-2}\exp\left(-s^2\right)\mathrm{d}s, \quad z > 0,\end{aligned}$$

we obtain

$$\tilde{\mathcal{K}}_3(\tau, \rho_{c_3}; \sigma) = \frac{\rho_{c_3}}{\rho_{c_3} + 2b\sigma\tau} + r(\sigma),$$

where

$$r(\sigma) := b\sqrt{\tau\sigma}\exp\left(z_\sigma^2\right)\int_{z_\sigma}^\infty s^{-2}\exp\left(-s^2\right)\mathrm{d}s.$$

This implies

$$\left|\tilde{\mathcal{K}}_3(\tau, \rho_{c_3}; \sigma) - \frac{\rho_{c_3}}{\rho_{c_3} + 2b\sigma\tau}\right| = |r(\sigma)| \le Cz_\sigma^{-3} = O\left(\rho_{c_3}^{-3}\right) \tag{A.8}$$

as $\rho_{c_3} \to \infty$. Set

$$e^{-\frac{\lambda_s-\lambda_d}{1-\sigma}}\tilde{\mathcal{K}}_3(\tau, \rho_{c_3}; \sigma)\tilde{\mathcal{K}}_3(\tau, \rho_{c_3}; 1-\sigma) = g(\tau; \sigma) + l(\tau; \sigma), \tag{A.9}$$

where

$$\begin{aligned} l(\tau;\sigma) &:= e^{-\frac{\lambda_s-\lambda_d}{1-\sigma}}\left(\frac{\rho_{c_3}}{\rho_{c_3} + 2b\sigma\tau}r(1-\sigma) + \frac{\rho_{c_3}}{\rho_{c_3} + 2b(1-\sigma)\tau}r(\sigma) + r(\sigma)r(1-\sigma)\right),\\ g(\tau;\sigma) &:= e^{-\frac{\lambda_s-\lambda_d}{1-\sigma}}\frac{\rho_{c_3}}{\rho_{c_3} + 2b\sigma\tau}\frac{\rho_{c_3}}{\rho_{c_3} + 2b(1-\sigma)\tau}. \end{aligned} \tag{A.10}$$

Based on (7.9), we split $I_{\lambda_{d,s}}$ of (A.3) into

$$I_{\lambda_{d,s}}(\tau) := I_d^a(\tau) + R_d^r(\tau), \tag{A.11}$$

where

$$\begin{aligned} I_d^a(\tau) &:= \int_0^{1/2} ((1-\sigma)\sigma)^{-\frac{3}{2}} e^{-\frac{\lambda_d}{(1-\sigma)\sigma}} g(\tau;\sigma)\,\mathrm{d}\sigma, \\ R_d^r(\tau) &:= \int_0^{1/2} ((1-\sigma)\sigma)^{-\frac{3}{2}} e^{-\frac{\lambda_d}{(1-\sigma)\sigma}} l(\tau;\sigma)\,\mathrm{d}\sigma. \end{aligned} \tag{A.12}$$

By (7.8), we note that R_d^r is a remainder term of $I_{\lambda_{d,s}}$ in (7.11) as $\rho_{c_3} \to \infty$. Further, we split I_d^a by applying the Taylor theorem to g of (7.10) at the center $\sigma = 1/2$. Then, we obtain

$$g(\tau;\sigma) = g(\tau;1/2) + \partial_\sigma g(\tau,\theta_\sigma)\left(\sigma - \frac{1}{2}\right) \quad \text{with} \quad 0 < \theta_\sigma < 1/2,$$

and

$$I_d^a(\tau) := \int_0^{1/2} ((1-\sigma)\sigma)^{-\frac{3}{2}} e^{-\frac{\lambda_d}{(1-\sigma)\sigma}} \left[g(\tau;1/2) + \partial_\sigma g(\tau,\theta)\left(\sigma - \frac{1}{2}\right)\right] \mathrm{d}\sigma. \tag{A.13}$$

We decompose $I_d^a(\tau)$ into $I_d^a(\tau) = I_d(\tau) + R_d(\tau)$, where

$$I_d(\tau) := \int_0^{1/2} ((1-\sigma)\sigma)^{-\frac{3}{2}} e^{-\frac{\lambda_d}{(1-\sigma)\sigma}} g(\tau;1/2)\,\mathrm{d}\sigma,$$

and

$$R_d(\tau) := \int_0^{1/2} ((1-\sigma)\sigma)^{-\frac{3}{2}} e^{-\frac{\lambda_d}{(1-\sigma)\sigma}} \partial_\sigma g(\tau,\theta)\left(\sigma - \frac{1}{2}\right) \mathrm{d}\sigma.$$

By change of a variable, we obtain

$$\begin{aligned} I_d(\tau) &= g(\tau;1/2) \int_0^\infty \xi^{-\frac{1}{2}} e^{-\lambda_d(4+\xi)}\,\mathrm{d}\xi = g(\tau;1/2)\sqrt{\pi}\lambda_d^{-\frac{1}{2}} e^{-4\lambda_d} \\ &= \frac{2\sqrt{\pi\tau}}{|\rho_d - \rho_c|} e^{-\frac{|\rho_d-\rho_c|^2 + |\rho_s-\rho_c|^2}{2\tau}} \left(\frac{\rho_{c_3}}{\rho_{c_3} + b\tau}\right)^2, \end{aligned}$$

which determines the asymptotics in (7.7). By (7.5), we have $|\partial_\sigma g(\tau;\sigma)| < C$, which implies

$$\begin{aligned} |R_d(\tau)| &= \left| \int_0^{1/2} ((1-\sigma)\sigma)^{-\frac{3}{2}} e^{-\frac{\lambda_d}{(1-\sigma)\sigma}} \partial_\sigma g(\tau,\theta)\left(\sigma - \frac{1}{2}\right) \mathrm{d}\sigma \right| \\ &\le C \int_0^\infty e^{-\lambda_d(4+\zeta)} (\zeta + 4)^{-\frac{1}{2}}\,\mathrm{d}\zeta \\ &\le C\lambda_d^{-1} e^{-4\lambda_d} \quad \text{for} \quad \tau > 0. \end{aligned} \tag{A.14}$$

This implies R_d is a remainder term of I_d^a in (7.13), precisely,

$$C(\tau)\tau^{-2}|R_d(\tau)| = C(\tau)\tau^{-2} O\left(\lambda_d^{-1} e^{-2(\lambda_d+\lambda_s)}\right) = O\left(\tilde{u}_m^a(\tau)\rho_{c_3}^{-1}\right)$$

as $\rho_{c_3} \to \infty$. Then, by (A.1), (7.7), (7.11), and (7.13)-(7.14), we obtain

$$\begin{aligned}\tilde{u}_m(\tau) &= C(\tau)\tau^{-2}(I_{\lambda_{d,s}}(\tau) + I_{\lambda_{s,d}}(\tau))\\ &= C(\tau)\tau^{-2}(\,[I_d^a(\tau) + R_d^r(\tau)] + [I_s^a(\tau) + R_s^r(\tau)]\,)\\ &= C(\tau)\tau^{-2}\,[I_d(\tau) + I_s(\tau)] + C(\tau)\tau^{-2}O\Big(R_d(\tau) + R_s(\tau)\Big)\\ &= \tilde{u}_m^a(\tau) + O\left(\tilde{u}_m^a(\tau)\rho_{c_3}^{-1}\right) \qquad \text{(A.15)}\end{aligned}$$

as $\rho_{c_3} \to \infty$. This implies (7.6), and the proof of Theorem 7.2 is complete. □

Author contributions

J. Eom developed the theoretical framework, derived the analytical results, and contributed to the mathematical analysis of the proposed method. J. Kim developed the methodology, designed and implemented the numerical experiments, performed the computational simulations, and analyzed the experimental results. H. Son developed the methodology, supervised the research, provided conceptual guidance, and contributed to the interpretation of the results. All authors contributed to the writing of the manuscript and approved the final version.

Use of Generative-AI tools declaration

The authors declare that AI tools were used only for grammar and language checking during the preparation of this article. No AI tools were used to generate scientific content, analyses, results, or conclusions.

Acknowledgement

Junyong Eom was supported by the JSPS KAKENHI (Grant Number 25K17291). Hwijae Son was supported by Basic Science Research Program through the National Research Foundation of Korea (NRF) funded by the Ministry of Education(RS-2024-00462755, RS-2026-25491905)

Conflict of interest

All authors declare no conflicts of interest in this paper.

References

1. Y. Liu, W. Ren, H. Ammari, Robust reconstruction of fluorescence molecular tomography with an optimized illumination pattern, *Inverse Probl. Imag.*, **14** (2020), 535–568. https://doi.org/10.3934/ipi.2020025
2. M. Mycek, B. Pogue, *Handbook of Biomedical Fluorescence*, Marcel Dekker, New York, 2003.
3. V. Ntziachristos, C. Tung, C. Bremer, R. Weissleder, Fluorescence molecular tomography resolves protease activity in vivo, *Nat. Med.*, **8** (2002), 757–761. https://doi.org/10.1038/nm729

4. H. Jiang, *Diffuse optical tomography: principles and applications*, CRC Press, Boca Raton, 2010.
5. H. Jiang, *Fluorescence Molecular Tomography: Principles and Applications*, Springer, Cham, Switzerland, 2022.
6. J. Hebden, R. Kruger, K. Wong, Time resolved imaging through a highly scattering medium, *Appl. Opt.*, **30** (1991), 788–794. https://doi.org/10.1364/AO.30.000788
7. J. Liu, M. Machida, G. Nakamura, G. Nishimura, C. Sun, On fluorescence imaging: The diffusion equation model and recovery of the absorption coefficient of fluorophores, *Sci. China Math.*, **65** (2022), 1179–1198.
8. V. Ntziachristos, R. Weissleder, Experimental three-dimensional fluorescence reconstruction of diffuse media by use of a normalized Born approximation, *Opt. Lett.*, **26** (2001), 893–895. https://doi.org/10.1364/OL.26.000893
9. N. Ducros, L. Hervé, A. Da Silva, J. M. Dinten, F. Peyrin, A comprehensive study of the use of temporal moments in time-resolved diffuse optical tomography: part i. theoretical material, *Phys. Med. Biol.*, **54** (2009), 7089–7105. https://doi.org/10.1088/0031-9155/54/23/004
10. D. Hall, G. Ma, F. Lesage, Y. Wang, Simple time–domain optical method for estimating the depth and concentration of a fluorescent inclusion in a turbid medium, *Opt. Lett.*, **29** (2004), 2258–2260. https://doi.org/10.1364/OL.29.002258
11. S. Chen, J. Eom, G. Nakamura, G. Nishimura, Approximate peak time and its application to time-domain fluorescence diffuse optical tomography, *Commun. Anal. Comput.*, **1** (2023), 379–406. https://doi.org/10.1126/science.adg7885
12. S. Chen, J. Eom, G. Nakamura, G. Nishimura, Direct inversion scheme of time-domain fluorescence diffuse optical tomography by asymptotic analysis of peak time, *Inverse Probl. Imag.*, 2026. In press.
13. S. Chen, J. Eom, G. Nakamura, G. Nishimura, Approximate peak time and a global reconstruction algorithm for time-domain fluorescence diffuse optical tomography, *J. Inverse Ill-Posed Probl.*, 2026. In press.
14. N. Ducros, A. Da Silva, L. Hervé, J. M. Dinten, F. Peyrin, A comprehensive study of the use of temporal moments in time-resolved diffuse optical tomography: part ii. three-dimensional reconstructions, *Phys. Med. Biol.*, **54** (2009), 7107–7119. https://doi.org/10.1088/0031-9155/54/23/005
15. A. Laidevant, A. Da Silva, M. Berger, J. Boutet, J. M. Dinten, A. C. Boccara, Analytical method for localizing a fluorescent inclusion in a turbid medium, *Appl. Opt.*, **46** (2007), 2131–2137. https://doi.org/10.1364/AO.46.002131
16. S. Lam, F. Lesage, X. Intes, Time domain fluorescent diffuse optical tomography: Analytical expressions, *Opt. Express*, **13** (2005), 2263–2275. https://doi.org/10.1364/OPEX.13.002263
17. J. Eom, G. Nakamura, G. Nishimura, C. Sun, Local analysis for locating a single point target in time-domain fluorescence diffuse optical tomography, *Differ. Integral Equ.*, **37** (2024), 27–58.
18. H. Son, M. Lee, A PINN approach for identifying governing parameters of noisy thermoacoustic systems, *J. Fluid Mech.*, **984** (2024), A21.

19. S. W. Cho, H. Son, Physics-informed deep inverse operator networks for solving pde inverse problems, In *International Conference on Learning Representations (ICLR)*, 2025.